Conductivity and dissociation in liquid metallic hydrogen and implications for planetary interiors

Mohamed Zaghoo[a] and Isaac F. Silvera[a,1]

[a]Lyman Laboratory of Physics, Harvard University, Cambridge, MA 02138

Edited by Vladimir E. Fortov, Russian Academy of Sciences, Moscow, and approved September 7, 2017 (received for review May 12, 2017)

Liquid metallic hydrogen (LMH) is the most abundant form of condensed matter in our solar planetary structure. The electronic and thermal transport properties of this metallic fluid are of fundamental interest to understanding hydrogen's mechanism of conduction, atomic or pairing structure, as well as the key input for the magnetic dynamo action and thermal models of gas giants. Here, we report spectrally resolved measurements of the optical reflectance of LMH in the pressure region of 1.4–1.7 Mbar. We analyze the data, as well as previously reported measurements, using the free-electron model. Fitting the energy dependence of the reflectance data yields a dissociation fraction of 65 ± 15%, supporting theoretical models that LMH is an atomic metallic liquid. We determine the optical conductivity of LMH and find metallic hydrogen's static electrical conductivity to be 11,000–15,000 S/cm, substantially higher than the only earlier reported experimental values. The higher electrical conductivity implies that the Jovian and Saturnian dynamo are likely to operate out to shallower depths than previously assumed, while the inferred thermal conductivity should provide a crucial experimental constraint to heat transport models.

liquid metallic hydrogen | phase transitions | planetary interiors

Liquid metallic hydrogen (LMH) is the benchmark Coulomb system that is the simplest and the lightest of all liquid metals. However, despite its apparent simplicity and fundamental significance, its thermodynamic and transport properties continue to pose outstanding challenges. Unlike other alkali metals, atomic metallic hydrogen is exceptional in possessing no bound electrons. Moreover, the low mass of its protonic system gives rise to a substantial zero-point motion. LMH is ubiquitous in the universe, making up about 60–70% of our solar planetary structure and the vast interiors of extrasolar giant planets (1).

In recent decades remarkable progress has been made in determining dense hydrogen's thermodynamic equation of state in the region relevant to planetary conditions (1, 2). However, the transport properties of LMH remain less well understood (2, 3). A key long-standing issue that pertains to these properties is the mechanism of electronic conduction: thermal excitation of carriers across a reduced mobility gap (4–6) versus conduction by free electrons in an atomic system (7, 8). The central question is whether metallization at these conditions occurs in the molecular phase or if it proceeds by dissociation into a conducting atomic phase (2). Accurate determination of the plasma frequency, and thus the carrier density, from the reflectance, as well as the density dependence of the optical conductivity, are experimental probes that can distinguish between these two models of metallization (5).

The confluence of quantum and thermal effects, as well as the strong coupling between the electrons and the protons, make it difficult to accurately calculate electrical and thermal conductivity. Theoretical models have to rely on different assumptions about the ionic system structure (7, 9, 10), the degree of ionization (3, 10, 11), and proton–proton correlations (8), all of which remain challenging to adequately describe. Ab initio density-functional theory (DFT) simulations differ substantially in their calculated conductivities, depending on the functionals used (12) (see also discussions in the supporting information of ref. 13). Experimentally, pioneering shock-wave experiments have reported plateauing of electrical conductivity at values around 2,000 S/cm in the region 1.4–1.8 Mbar (6). It was argued that the plateau of conductivity was due to thermal smearing of the band gap and that metallization occurs in the molecular phase with 5–10% dissociation fraction (5, 6). We note that the reported values of conductivity are a factor of 3 less than the Mott–Ioffe–Regal (MIR) minimum metallic conductivity criterion, 6,000 S/cm (4, 14), and a factor of 5–10 lower than values predicted with different theoretical models for fully ionized metallic liquids (3, 5, 7–9, 15).

Here we report measurements of the optical conductivity of bulk LMH at planetary interior conditions in the pressure region of 1.4–1.7 Mbar and measured temperatures of 1,800–2,700 K, which are comparable to the conditions studied by Nellis et al. (4, 5) and Weir et al. (6), but at higher temperatures than those inferred for deuterium studies by Knudson et al. (13). Pressurized hydrogen was pulse-laser heated and time-resolved spectroscopy was used to measure the optical reflectance in eight optical runs using an experimental setup shown in *Supporting Information*. Unlike previous static and shock-wave work, the energy dependence of optical reflectance was measured simultaneously with temperature, thus removing systematic uncertainties that arise from separate measurements of reflectance and temperature. The duration of the laser pulse, 290 ns, is sufficiently long to achieve local thermal equilibrium yet short enough to inhibit sample diffusion into metallic gasket and diamonds.

Optical reflectance of hot dense hydrogen samples was measured simultaneously or separately (in different experiments) at three wavelengths: 514, 633, and 980 nm. We observed an abrupt increase in reflectance above a certain transition temperature consistent with previous results (16) (Fig. 1). At threshold, the LMH film is thin and semitransparent (*Supporting Information*).

Significance

Liquid metallic hydrogen (LMH) is a fundamental system in condensed matter sciences and the main constituent of gas giant planets. Because of exceptional challenges in experimentation and theory, its transport properties remained poorly understood. We have conducted experimental determination of the optical conductivity of bulk LMH using spectrally resolved reflectance measurements on statically compressed and heated hydrogen. Metallic hydrogen's mechanism of metallization is largely dissociative to an atomic state, rather than the previously held experimental model, ionization of molecules. We find that LMH's electrical conductivity is substantially higher, a factor of 6–8, than the only experimentally reported value in the literature, measured in the dc limit. The implications of the current results to Jovian giants planetary models are discussed.

Author contributions: M.Z. and I.F.S. designed research, performed research, analyzed data, and wrote the paper.

The authors declare no conflict of interest.

This article is a PNAS Direct Submission.

[1]To whom correspondence should be addressed. Email: silvera@physics.harvard.edu.

This article contains supporting information online at www.pnas.org/lookup/suppl/doi:10.1073/pnas.1707918114/-/DCSupplemental.

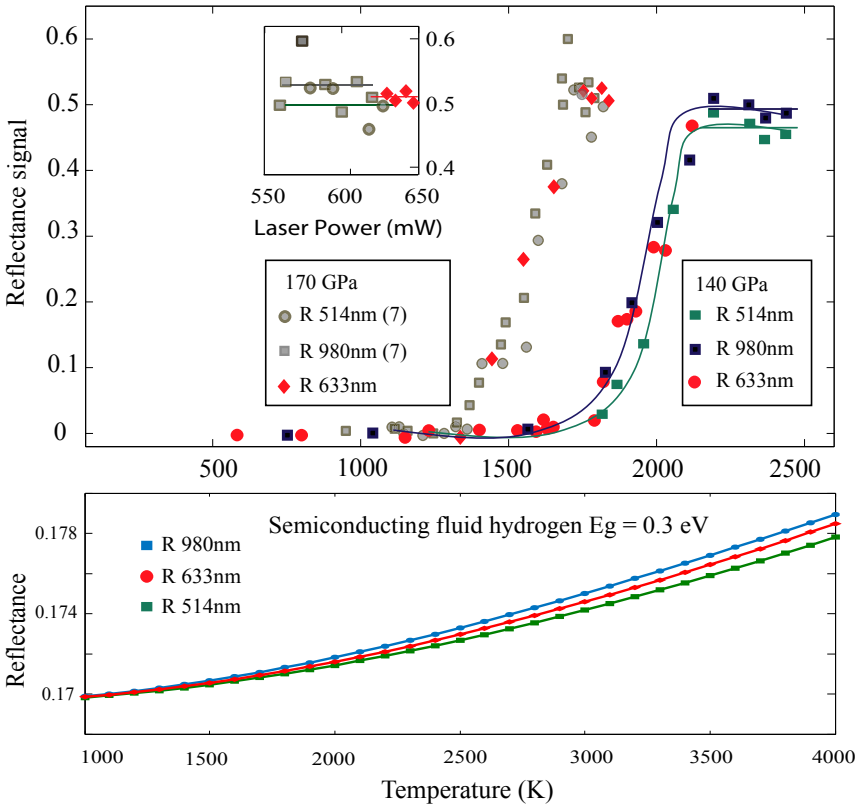

Fig. 1. Dense hydrogen reflectance as a function of temperature plotted for three wavelengths: 514, 633, and 980 nm. Above a certain transition temperature, liquid hydrogen metallizes and reflects incident probe light. Lines are guides to the eye. The relatively larger scatter in the 170 GPa LMH bulk reflectance data, shown in detail (*Inset*), is because each wavelength measurement was collected separately, while for 140 GPa reflectances at 514 and 980 nm were measured simultaneously. (*Bottom*) For comparison, calculations are shown of expected reflectance due to thermally activated carriers plotted against temperature if hydrogen were semiconducting with a 0.3-eV band gap. The sharp step is absent for this case.

As the laser power is increased, the film heats and thickens until the transmission is essentially zero and reflection corresponds to that of a bulk metal. This value of reflectance is consistent with values obtained in previous shock-wave and static experiments (13, 16–18). Once the reflectance saturates, it is weakly dependent on temperature, as expected in a degenerate metallic system. We further compare our observed reflectance in Fig. 1 to that expected for hydrogen if it was semiconducting with a finite gap and the carriers are thermally activated, as previously suggested (6). The strong disagreement with our measurements enables us to reject a semiconductor model.

Optical reflectance measurements are amenable to a Fresnel analysis. The measured reflectance at a given frequency is $R(\omega)=|(N_D-N_H)/(N_D+N_H)|^2$, where N_D is the index of refraction of molecular hydrogen/diamond layer and N_H is the complex index of refraction of LMH. The observed saturation of optical reflectance, conditions of electron degeneracy ($T << T_f$, the Fermi temperature; *Supporting Information*), and the characteristic wavelength dependence of the conduction are important conditions for application of the free-electron model. We have thus analyzed the optical response of LMH, only in the limit of saturated reflectance, using the Drude free-electron model, which has previously been extensively used for LMH (7, 15, 19). Use of this model is further justified below. In this model, $N_H^2=1-\omega_p^2/(\omega^2+j\omega/\tau)$, where ω_p is the plasma frequency, which is directly related to the carrier density n by $\omega_p^2=4\pi ne^2/m_e$, and τ is the electron relaxation time. We define a dissociation/ionization fraction Z as the ratio of the carrier to ion density. Thus, if all molecules are dissociated, $Z=1$, while if all molecules are ionized or half atomic-molecular, $Z=1/2$. Accurate measurements of $R(\omega)$ can thus be used to determine ω_p and τ from which the carrier density or the degree of dissociation can be deduced. We performed a least-squares nonlinear fit of our measured $R(\omega)$ to extract these parameters (Fig. 2).

We have determined the Drude parameters at 140 and 170 GPa. At 140 GPa, our reflectance data are best fit to ω_p =20.4 ± 1.6 eV and $\tau=1.3\pm0.2\times10^{-16}$ s, yielding a dissociation fraction Z of 0.65 ± 0.15. We determine σ_{dc} = 11,000 ± 1,100 S/cm, a factor of 2 higher than Mott's minimum metallic conductivity at this pressure (*Supporting Information*). At 170 GPa, our data, as well as those reported in ref. 16, are best fit to $\omega_p=21.8\pm2.8$ eV and $\tau=1.6\pm0.3\times10^{-16}$ s, yielding a $Z=0.57\pm0.14$. This corresponds to $\sigma_{dc}=15{,}500\pm1{,}500$ S/cm. We contrast our optical reflectance and the Drude fits to that expected for LMH using the minimum relaxation times τ_{min} prescribed by the MIR limit. Such a limit, which is often employed by shock-wave experiments (4), cannot account for the observed reflectance of LMH shown in Fig. 2.

Several ab initio calculations have suggested that at the onset of the insulator–metal transition, the fluid may exhibit a non-free-electron-like density of states (7, 12, 19). Our optical data present experimental evidence for such behavior, where we show that in the transition onset region in which the reflectance is rapidly rising, the data cannot be fit to the Drude model (Fig. 2, *Top Left*). As the dissociation fraction increases, LMH becomes more Drude-like and the free-electron character is established. This result provides a further justification for the validity of the Drude model in the degeneracy region. The real part of the optical conductivity is plotted in Fig. 2, where the determined relaxation time is assumed to be frequency independent. We have investigated a possible deviation from this assumption through the empirical Smith–Drude (SD) model (20). In this model, a backscattering term is introduced that

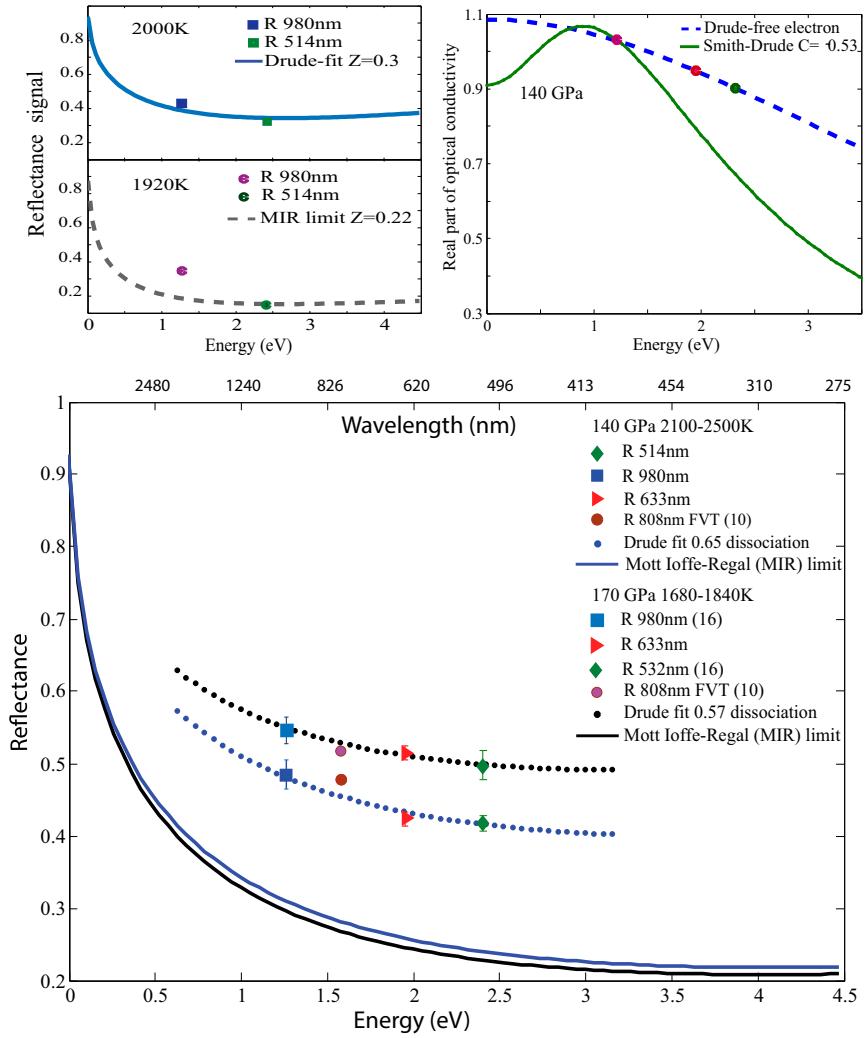

Fig. 2. (*Bottom*) Bulk LMH reflectance as a function of energy or wavelength is plotted for 140- and 170-GPa pressures in the region where reflectance saturates. Optical reflectance is higher for increasing pressures as expected in dissociation-induced metallization. The Drude fit to the experimental data (filled circles) is determined from a least-squares fit to the energy dependence of measured reflectance. The solid lines are the calculated reflectance using the MIR limit for the same determined plasma frequency. Systematics are discussed in *Supporting Information*. (*Top Left*) LMH reflectance signal below the saturation region at 140 GPa at two temperatures. At 1,920 K, with low reflectance corresponding to the onset of the transition, the wavelength dependence cannot be fit with the Drude model; however, at higher temperatures and reflectance, as the degree of dissociation increases, the system becomes more free-electron-like, resulting in a better fit. Systematics are discussed in *Supporting Information*. (*Top Right*) Real part of the optical conductivity plotted as a function of energy for two different models: the Drude free-electron versus the empirical Smith–Drude (20) model with a backscattering term. Solid circles represent the determined values for optical conductivity. We show that a non-Drude-like behavior below 1.2 eV will only have a small effect in the determined conductivity (*Supporting Information*).

shifts the Drude Lorentzian peak to a nonzero frequency. An effort to fit to the SD model is shown in Fig. 2, *Top*. A best fit is quite poor and only crosses one data point on the curve, shifting the peak to the infrared (below our measured 1.2 eV) and will only have a minor effect on the determined dc conductivity.

It is instructive to compare our LMH Drude parameters to those recently reported for the Wigner–Huntington transition at ∼500 GPa and cryogenic temperatures (21). The higher plasma frequency, ∼30 eV, found from these experiments is consistent with the higher carrier densities at the higher pressures ($\omega_p \propto \sqrt{n}$). Moreover, the difference in the relaxation times, a factor of 6 shorter for LMH, is likely related to the temperature difference between LMH at ∼2,000 K and the cryogenic temperature metallic phase. We further compare our results to those obtained experimentally for warm dense xenon. In those shock-wave experiments, the energy dependence of the optical reflectance in compressed xenon was measured as a function of pressure and Brewster angles (22, 23). Fitting the free-electron model to this pressure dependence yielded relaxation times on the order of 2.655×10^{-15}–3.6×10^{-15} s (22). These values are almost an order of magnitude longer than those obtained from our experiments. Moreover, it is unclear whether those longer relaxation times are attributed to an experimental effect, related to broadening of shock-wave fronts, or to the physics of xenon at the reported conditions (24).

In highly degenerate systems, such as LMH, thermal transport is very likely dominated by conduction electrons. Thermal conductivity could thus be related to electrical conduction through the Lorentz proportionality constant. We have calculated the electronic contribution to thermal conductivity of LMH using the Wiedemann–Franz law, whose application is all the more supported by theoretical models (3).

In Fig. 3, we compare our electrical and thermal conductivity values to several theoretical predictions using various models of different degrees of sophistication. Our LMH dc conductivities and

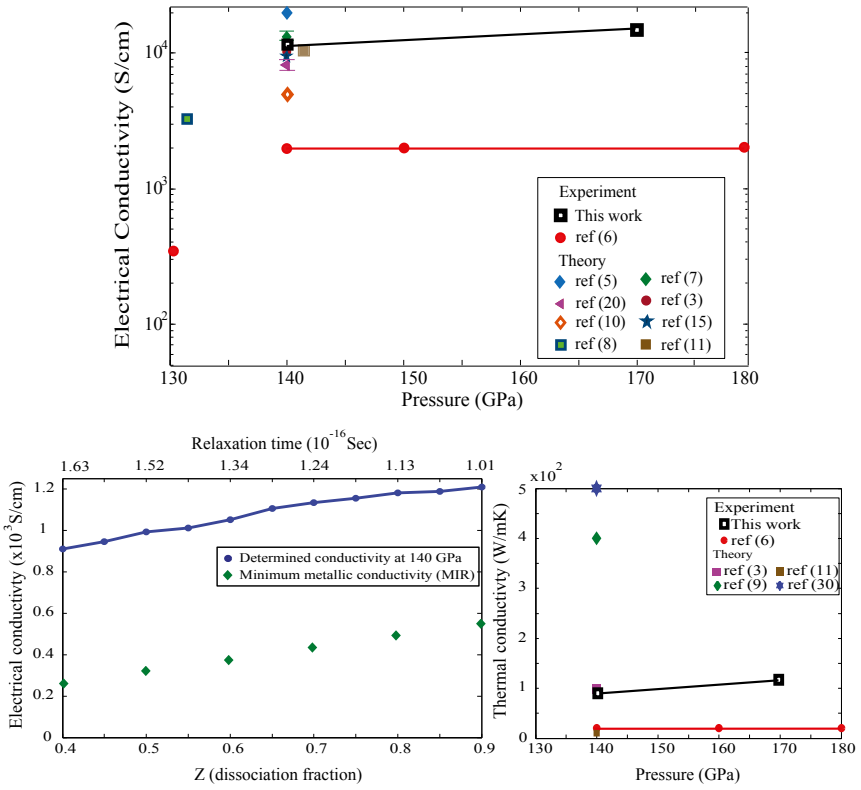

Fig. 3. (*Top*) Electrical conductivity of LMH as a function of pressure compared with several theoretical predictions on a logarithmic scale. Uncertainty is about 10–15% in the experimental data. (*Bottom Right*) Thermal conductivity of LMH as a function of pressure at 4,000 K determined from the Wiedemann–Franz law, compared with several theoretical predictions. (*Bottom Left*) The electrical conductivity of LMH determined from the fits to our measured data, by fixing the plasma frequency, plotted as a function of relaxation times and dissociation fraction. The diamond symbols are the minimum metallic conductivity (MIR) criterion calculated as a function of density using Mott's formula $\sigma_{min} = e^2/3ha$ (14). The line is a guide to the eye.

relaxation times are in very good agreement with DFT-molecular dynamics (7, 15) and correlated electron-ion Monte Carlo (CEIMC) calculations that predict $\sigma_{dc} = 13{,}000$ S/cm and $\tau = 3.0 \pm 0.1 \times 10^{-16}$ s and $\sigma_{dc} = 8{,}600$ S/cm and $\tau = 3.1 \pm 0.3 \times 10^{-16}$ s, respectively, as well as those calculated for fully ionized hydrogen plasmas, albeit at higher T (11).

Our electrical conductivities are a factor of 6–8 higher than those previously reported by Weir et al. (6). The uncertainties in those measurements ranged from 25 to 50% (6). The exact origin of discrepancy is unknown, with temperature being an unlikely factor, since our optical data show a clear saturation as a function of increasing T. Moreover, assuming that conductivity may suffer a reduction at increasing T, its limiting value (MIR limit) is still three times higher than reported in ref. 6. Possible sources of uncertainties for those measurements could include inaccuracies in estimating the shocked cryogenic cell thickness at the highest compression, the value that relates the measured resistance to resistivity (*Supporting Information*). We note that our reflectance measurements in the bulk limit are insensitive to this consideration. Experiments on LMH should, in principle, observe increasing reflectance as a function of density, provided the temperatures are relatively low.

Within experimental uncertainties, the energy dependency of the optical reflectances is well described by the Drude model. A large dissociation fraction within the free-electron model is required to best fit that energy dependence. We note that irrespective of our choice of τ, a 5–10% dissociation fraction inferred from Nellis et al. (4) and Weir et al. (6) cannot fit our reflectance data (19) (Fig. S7). Our observed increasing optical conductivity as a function of pressure is also consistent with this conclusion, where a rising density of free electrons leads to a further increase in conductivity. A negative slope of the metallization phase line revealed from our data is also consistent with the dissociation model; the dissociation energy decreases with density and thus the transition temperature decreases (2). In contrast to the interpretation proposed in previous experiments (4, 6, 13), LMH at the conditions of our experiments is largely atomic and degenerate. The transition is also abrupt and reflectance rises to metallic-like values, ~0.3, within ~100 K (*Supporting Information*). Additionally, we have not observed any concomitant interband transitions in the frequency range investigated, consistent with a first-order transition. Our results thus do not support a conduction mechanism by thermal smearing of a reduced Mott–Hubbard gap. A mechanism of band overlap in the molecular phase has also been suggested where one electron per molecule contributes to conduction or the equivalent of 50% dissociation fraction (5). Within the uncertainties of our fit, the current measurements cannot conclusively distinguish between a mixed atomic-molecular metal and a fully molecular metal. Additional low-frequency reflectance measurements could resolve this uncertainty.

Apart from their fundamental significance, the determined properties of LMH have important consequences to dynamo and thermal models of hydrogen-rich planets. These models await new magnetic and gravitational observations by the Juno and Cassini space probes. The gas giants, which are ~90% hydrogen, are composed of a fluid hydrogen–helium envelope and possibly a dense central core (1). As the atmosphere is entered, P and T increase until a layer of LMH is encountered. The conductivity of LMH reported here is representative of P-T conditions at ~0.84 of Jupiter's radius, R_J, and 0.63 of Saturn's radius, R_S (25). It corresponds to a magnetic diffusivity of $\sim 0.56 \times 10^4$ cm^2/s, a factor of 8 lower than previously inferred from Weir et al. (6), and now roughly similar to new estimates of Earth's iron core. The addition of 9% helium is most likely unimportant for these conductivity

estimates (*Supporting Information*). Our experimental values are also considerably higher than the ab initio transport values calculated along the Jovian adiabat at similar pressures (26), where the used DFT functionals employed evidently underestimate conduction. Since the interaction of the magnetic field with the fluid flow (Ohmic dissipation) scales linearly with electrical conductivity, higher conductivities should result in substantially more dissipation at this transition depth than currently assumed. This should revise recent estimates on the penetration depth of the zonal winds to even shallower bounds than their quoted 0.84 R_J or 0.63 R_S (25, 27). Precise gravitational measurements of low-order harmonics expected by Cassini should further confine this boundary. The Jovian dynamo is also most likely to operate out to a pressure that is much lower than that at 0.84 R_J, into a regime where hydrogen is not fully ionized. If metallization along the Jupiter adiabat is continuous, as both theory and previous experiments suggest, then the depth at which hydrogen conductivity reaches values corresponding to a magnetic diffusivity sufficient to sustain the dynamo ($\sim 10^7$ cm^2/s) may extend to more than $R_J = 0.91$. This dynamo depth is much lower than most previous estimates (28–30) and even likely lower than the value inferred by recent dynamo simulations (31, 32) based on the ab initio transport results (26). Since the effect of the dynamo origin depth on the observed magnetic spectrum is mostly manifested at the higher harmonic contributions, the Juno magnetic measurements should provide much tighter observational constraints to future dynamo models, where electrical conductivity profiles remain the key input. In this respect, the dissociation-based picture revealed in this article is particularly important as it means that LMH transport coefficients should scale with increasing density or Jovian radius, consistent with our observation for optical conductivity. This is remarkable for most anelastic dynamo simulations that otherwise prescribe a characteristic constant conductivity for depths below the metallic transition region (29).

Our inferred thermal conductivity values are also considerably lower by a factor of 4–6 than the theoretical estimates in current use for heat-transport models of Jovian-like planets (9, 33). Revised estimates should thus provide a crucial experimental benchmark for future models, particularly those proposing layered convection as a likely origin for Saturn's strikingly higher luminosity (34) or the anomalously large radius of several extrasolar transiting hot Jupiters (35).

Materials and methods are available as *Supporting Information*.

ACKNOWLEDGMENTS. We thank Ashkan Salamat, Ranga Dias, Ori Noked, and Rachel Husband as well as Bill Nellis for discussions. NSF Grant DMR-1308641, the DOE Stockpile Stewardship Academic Alliance Program, Grant DE-NA0001990, and NASA Earth and Space Science Fellowship Program, Award NNX14AP17H, supported this research. Preparation of diamond surfaces was performed in part at the Center for Nanoscale Systems (CNS), a member of the National Nanotechnology Infrastructure Network, which is supported under NSF Award ECS-0335765. CNS is part of Harvard University.

1. Guillot T (2005) The interiors of giant Planets: Models and outstanding questions. *Annu Rev Earth Planet Sci* 33:493–530.
2. McMahon JM, Morales MA, Pierleoni C, Ceperley DM (2012) The properties of hydrogen and helium under extreme conditions. *Rev Mod Phys* 84:1607–1653.
3. Holst B, French M, Redmer R (2011) Electronic transport coefficients from ab initio simulations and application to dense liquid hydrogen. *Phys Rev B* 83:235120.
4. Nellis WJ, Weir ST, Mitchell AC (1999) Minimum metallic conductivity of fluid hydrogen at 140 GPa (1.4 Mbar). *Phys Rev B* 59:3434–3449.
5. Nellis WJ, Louis AA, Ashcroft N (1998) Metallization of fluid hydrogen. *Philos Trans R Soc London, A* 356:119–138.
6. Weir ST, Mitchell AC, Nellis WJ (1996) Metallization of fluid molecular hydrogen at 140 GPa (1.4 Mbar). *Phys Rev Lett* 76:1860–1863.
7. Pfaffenzeller O, Hohl D (1997) Structure and electrical conductivity in fluid high-density hydrogen. *J Phys Condens Matter* 9:11023–11034.
8. Lenosky TJ, Kress JD, Collins LA, Kwon I (1997) Molecular-dynamics modeling of shock-compressed liquid hydrogen. *Phys Rev B* 55:R11907–R11910.
9. Stevenson DJ, Salpeter EE (1977) The phase diagram and transport properties for hydrogen-helium fluid planets. *Astrophys J* 35:221–237.
10. Holst B, Redmer R, Desgreniers S (2008) Thermophysical properties of warm dense hydrogen using quantum molecular dynamics simulations. *Phys Rev B* 77:1804201.
11. Reinholz H, Redmer R, Nagel S (1995) Thermodynamic and transport properties of dense hydrogen plasmas. *Phys Rev E Stat Phys Plasmas Fluids Relat Interdiscip Topics* 52:5368–5386.
12. Morales MA, Pierleoni C, Schwegler E, Ceperley DM (2010) Evidence for a first-order liquid-liquid transition in high-pressure hydrogen from ab initio simulations. *Proc Natl Acad Sci USA* 107:12799–12803.
13. Knudson MD, et al. (2015) High-pressure physics. Direct observation of an abrupt insulator-to-metal transition in dense liquid deuterium. *Science* 348:1455–1460.
14. Mott NF (1972) Conduction in non-crystalline systems IX. The minimum metallic conductivity. *Philos Mag* 26:1015–1026.
15. Hood RQ, Galli G (2004) Insulator to metal transition in fluid deuterium. *J Chem Phys* 120:5691–5694.
16. Zaghoo M, Salamat A, Silvera IF (2016) Evidence for a first-order phase transition to metallic hydrogen. *Phys Rev B* 93:155128–155135.
17. Celliers PM, et al. (2000) Shock-induced transformation of liquid deuterium into a metallic fluid. *Phys Rev Lett* 84:5564–5567.
18. Loubeyre P, et al. (2012) Extended data set for the equation of state of warm dense hydrogen isotopes. *Phys Rev B* 86:144115.
19. Lin F, et al. (2009) Electrical conductivity of high-pressure liquid hydrogen by quantum Monte Carlo methods. *Phys Rev Lett* 103:256401.
20. Smith NV (2003) Classical generalization of the Drude formula for the optical conductivity. *Phys Rev B* 64:155106–155112.
21. Dias RP, Silvera IF (2017) Observation of the Wigner-Huntington transition to metallic hydrogen. *Science* 355:715–718.
22. Mintsev VB, Zaporogets YB (1989) Reflectivity of dense plasma. *Contrib Plasma Phys* 29:493–501.
23. Reinholz H, et al. (2003) Frequency-dependent reflectivity of shock-compressed xenon plasmas. *Phys Rev E Stat Nonlin Soft Matter Phys* 68:036403.
24. Norman G, Saitov I, Stegailov V, Zhilyaev P (2015) Ab initio calculation of shocked xenon reflectivity. *Phys Rev E Stat Nonlin Soft Matter Phys* 91:023105.
25. Liu J, Schneider T, Fletcher L (2014) Constraining the depth of Saturn's zonal winds by measuring thermal and gravitational signals. *Icarus* 239:260–272.
26. French M, et al. (2012) Ab initio simulations for material properties along the Jupiter Adiabat. *Astrophys J, Suppl Ser* 202.
27. Liu J, Schneider T, Kaspi Y (2013) Predictions of thermal and gravitational signals of Jupiter's deep zonal winds. *Icarus* 224:114–125.
28. Guillot T, Stevenson DJ, Hubbard WB, Saumon D (2004) The interior of Jupiter. *Jupiter: The Planet, Satellites, and Magnetosphere* (Cambridge Univ Press, Cambridge, UK), pp 35–57.
29. Stanley S, Glatzmaier G (2010) Dynamo models for planets other than Earth. *Space Sci Rev* 152:617–649.
30. Jones CA (2011) Planetary magnetic fields and fluid dynamos. *Annu Rev Fluid Mech* 43:583–614.
31. Duarte LD, Gastine T, Wicht J (2013) Anelastic dynamo models with variable electrical conductivity: An application to gas giants. *Phys Earth Planet Inter* 222:22–34.
32. Jones CA (2014) A dynamo model of Jupiter's magnetic field. *Icarus* 241:148–159.
33. Potekhin AY (1999) Electron conduction in magnetized neutron star envelopes. *Astron Astrophys* 351:787–797.
34. Leconte J, Chabrier G (2013) Layered convection as the origin of Saturn's luminosity anomaly. *Nat Geosci* 6:347–350.
35. Chabrier G, Baraffe I (2007) Heat transport in giant (exo) planets: A new perspective. *Astrophys J* 661:81–84.
36. Dzyabura V, Zaghoo M, Silvera IF (2013) Evidence of a liquid–liquid phase transition in hot dense hydrogen. *Proc Natl Acad Sci USA* 110(20):8040–8044.
37. Mihailidi M, Xing Q, Yoo KM, Alfano RR (1994) Electron-phonon relaxation dynamics of niobium metal as a function of temperature. *Phys Rev B* 49:3207.
38. Evans W, Silvera IF (1998) Index of refraction, polarizability, and equation of state of solid molecular hydrogen. *Phys Rev B* 57:14105–14109.
39. Ioffe AF, Regel AR (1960) Non-crystalline, amorphous, and liquid electronic semiconductors. *Progress in Semiconductors*, ed Gibson AF (Heywood and Co., Ltd., London), Vol 4, pp 237–291.
40. Mao H, Hemley RJ (1994) Ultrahigh-pressure transitions in solid hydrogen. *Rev Mod Phys* 66:671–692.
41. Celliers P, et al. (2004) Electronic conduction in shock-compressed water. *Phys Plasmas* 11:L41.
42. Celliers PM, et al. (2010) Insulator-to-conducting transition in dense fluid helium. *Phys Rev Lett* 104:184503.
43. Millot M, et al. (2015) Shock compression of stishovite and melting of silica at planetary interior conditions. *Science* 347(6220):418–420.
44. Eggert J, et al. (2010) Melting temperature of diamond at ultrahigh pressure. *Nat Phys* 6:40–43.
45. Hicks DG, Celliers P, Collins G, Eggert J, Moon SJ (2003) Shock-induced transformation of Al2O3 and LiF into semiconducting liquids. *Phys Rev Lett* 91(3):035502–035506.
46. Nellis WJ, Mitchell AC, McCandless PC, Erskine DJ, Weir ST (1992) Electronic energy gap of molecular hydrogen from electrical conductivity measurements at high shock pressures. *Phys Rev Lett* 68:2937.
47. Lorenzen W, Holst B, Redmer R (2011) Metallization in hydrogen-helium mixtures. *Phys Rev B* 84:235109.
48. Christensen UR, Aubert J (2006) Scaling properties of convection-driven dynamos in rotating spherical shells and application to planetary magnetic fields. *Geophys J Int* 166(1):97–114.
49. Pozzo M, Davies C, Gubbins D, Alfe D (2012) Thermal and electrical conductivity of iron at Earth's core conditions. *Nature* 485:355–358.

Supporting Information

Zaghoo and Silvera 10.1073/pnas.1707918114

Hydrogen was pressurized in a diamond anvil cell (DAC) at room temperature using rhenium gaskets. Diamonds were coated with a 50-nm layer of alumina that acts as a diffusion barrier against hydrogen. Samples at static loads (fixed density) were pulse-laser heated using a Nd-yttrium aluminum garnet infrared laser (20-kHz repetition rate and 290-ns pulse widths) to peak temperatures as high as ∼2,700 K. Molecular hydrogen is transparent and will not absorb the laser energy. A thin (∼7 nm) semitransparent tungsten film that performs as a laser absorber was deposited on the alumina layer of one of the diamonds (and covered with a 5-nm protective layer of alumina). As the film is semitransparent, it enables optical measurements of reflectance and transmission of the LMH. The film was heated by the laser which conductively heats the hydrogen sample pressed against its surface (16, 36). The sample region of our DAC is shown in Fig. S1, as well as the reflectance geometry, which has undergone an important modification since our first observation of LMH (16). In our previous experiments only one laser-light optical measurement was possible at a time, resulting in large uncertainty of optical constants. In those measurements, there was a systematic uncertainty of ±50 K for measurement of temperature. Clearly from Fig. 1, the steep rise of reflectance can lead to large systematic uncertainties in reflectances at different wavelengths, and the wavelength dependence or reflectance is what is used to determine the optical constants. On the other hand, at higher temperatures or in the thick-film limit there is little variation of the reflectance corresponding to ±50 K temperature uncertainties. In the current experiment, we used wavelength filtering and separate detectors to simultaneously measure reflectance at two wavelengths (Fig. S1), along with the temperature, eliminating the systematic uncertainty in temperature. This allowed us to analyze reflectance in regions where it rapidly changes with temperature.

The hydrogen layer adjacent to the W film is in local thermal equilibrium with the W during this relatively long pulse, as electrons and translational motions thermalize within ∼10 ps (37). The energy/pulse, absorbed in the W film, is relatively small (∼0.005 mJ), so that the diamonds remain at room temperature on average. Pressure is determined by the shift of the Raman-active vibron of the hydrogen. The pressure was measured at room temperature before and after the heating run to ensure the integrity of the sample. Temperature was measured by pyrometry techniques, the details of which were thoroughly discussed in earlier work (36). However, in the interest of self-containment, we outline the basic principle of our measurement technique as well as further refinements in the current work. Thermal emission signals were collected on an InGaAs detector, sensitive in the 0.9–1.7-μm spectral region. Collection times ranged from 45 s at the very low laser powers to 180 ms at the highest powers; the signal was averaged over many heating pulses.

The energy flux of gray-body irradiance can be rewritten for a wavelength and temperature dependent emissivity as follow

$$F_\lambda \, \mathrm{d}\lambda = 15o\frac{T^4}{\pi^4}\frac{\lambda}{x}\frac{x^5}{e^x-1}\varepsilon(\lambda,T)d\lambda,$$

where $o = 2\pi^5k^4/15\ c^2h^3$, $x = hc/\lambda KT$, and $\varepsilon(\lambda,T)$ is the sample emissivity at normal incidence. In this form the emissivity accounts for deviations of the observed thermal radiation from ideal blackbody behavior.

To determine the true shape of the blackbody irradiance of heated samples, one needs to measure the transfer function, a function that accounts for the losses and chromatic aberrations introduced by the optical setup, as well as detector quantum efficiency. Besides correcting the spectral irradiance from our samples to the response of the optical system, the transfer function subsumes the absorber emissivity with its complex wavelength dependence as well as the measuring detector quantum efficiency. The signal includes components arising from the first- and second order of the diamond phonon Raman scattering, as well as diamond fluorescence. Since our aim is to determine the thermal radiation spectra required for the Planckian fitting, all of the various contributions to the collected spectra had to be separated.

Thus, the total signal has two components: the scattered background radiation assumed to have the same spectrum for all power, but amplitudes that scale with the laser power; and the blackbody contribution, which is nonlinear and when isolated can be fit to determine the temperature. Fig. S2 shows two examples for the raw corrected spectrum and the Planckian fits at two different temperatures below and above the transition at 140 GPa. The residuals from the best least-squares fit to the Planck curve define the uncertainty in the determined peak temperature. The uncertainty at those temperatures is on the order of 15–19 K.

At high pressures, the molecular hydrogen is a few micrometers thick, while we estimate that the heated part of the sample that metallizes in the bulk limit is of submicrometer thickness. More details of the experimental configuration, technique, and optical setup are described elsewhere (16).

Reflectance Analysis

Time-resolved reflectance measurements were conducted at fixed wavelengths of 514, 633, and 980 nm, using continuous wave solid-state lasers. The reflected light off of the W/hydrogen interface was monitored as a function of temperature and pressure using Si detectors with 2-ns rise times. At low temperatures, the W layer dominates reflectance when hydrogen is still in the molecular phase. Above a certain transition temperature T_c, the hydrogen sample metallizes and starts reflecting (Fig. S3). The transition to the metallic reflective state is abrupt and the reflectance rises up to ∼30%, metallic-like values, within ∼100–150 K. Increased heating thickens the metallic layer which reflects more light (Fig. S3). The thickening of the metallic layer is a function of the heating efficiency which depends on the focusing on the laser and the thermal boundaries/diffusivities of the molecular layer. Additional kinetic effects related to inhomogeneous heating might be present close to the metallization boundary, onset of reflectance. However, these effects should be small due to the high thermal conductivity of the metallic hydrogen.

Since the sample region exhibits thermo-transmittance, the reflectance above T_c is normalized to reflectance measured just below T_c. The phase line delineating this boundary between the insulating and metallic phase as well the thermodynamic pathway for the current experiments are shown in Fig. S4. Close to the transition region, the measured reflectance signal may include some contributions from the W layer if the LMH film is thin enough. As more energy is delivered to the LMH sample, its thickness grows, temperature increases, and this contribution becomes negligible (less than few percent). Once the LMH layer is thick enough, $R(\omega)$ plateaus at a fixed bulk value that is comparable to previous shock-wave experiments (13, 17, 18). The mean of $R(\omega)$ at that saturation limit is the experimentally reported value used for the Drude fit and the SD determines the uncertainty. In the bulk limit, the interface between the metallic and molecular hydrogen is much smaller than the wavelength of the probe light and thus it could be approximated as a specularly

smooth surface. At 140 GPa the index of refraction of solid molecular hydrogen, and to less than a percent fluid molecular hydrogen, is ~2.4 (38). This is close to that of diamond and so we treat the molecular hydrogen diamond as one interface (Fig. S1). We note that the choice of this pressure region to investigate metallic hydrogen bulk reflectance properties is thus convenient, as we do not have to deal with multilayer interfaces, and one can use the intensity approximation for analysis rather than a Fresnel analysis in which amplitudes of the electromagnetic waves are propagated through the cell (16).

Eight optical runs, monitoring $R(\omega)$ as a function of T, were conducted on two different samples, where $R(\omega)$ values of bulk LMH showed excellent reproducibility (Fig. S5). Some systematic uncertainties due to roughening of the W/hydrogen interface with time could have occurred, but should be rather small. The $R(\omega)$ data at 140 GPa were collected simultaneously at 980 and 514 nm, whereas measurements of $R(\omega)$ at 170 GPa were conducted separately but on the same sample. This has led to a better Drude fit at 140 GPa than at 170 GPa. Additional measurements at lower or higher frequency could further constrain the fits, but will not change the overall results. Fig. S6 shows the weighted least-squares fit at 140 GPa. The plasma frequency (carrier density) and the relaxation time were extracted from the fits using the Drude reflectance formula described in the main text.

The best fit to our reflectance results yields a dissociation fraction, $Z = 0.65 \pm 0.15$ with an R-square value of 0.95. Since the degree of dissociation is fundamental for understanding the metallization mechanism, we investigated the range of fitting parameters by imposing restrictions. For example, if we restrict the value of Z to 0.4–0.5, we find an R-square value of 0.70–0.90 and $\tau = 1.54 \pm 0.17 \times 10^{-16}$ s. At 170 GPa and 1,700 K, our reflectance data are best fit to an $\omega_p = 21.8 \pm 2.8$ eV and $\tau = 1.6 \pm 0.3 \times 10^{-16}$ s, yielding a dissociation fraction $Z = 0.57 \pm 0.14$.

Within the uncertainty in the fits, this dissociation fraction is comparable to that at 140 GPa at 2,500 K (Fig. S6). However, we note that the difference in temperature range where the optical data were fit might explain why it is not higher at increasing pressures. Since the static Drude electrical conductivity depends linearly on both the dissociation fraction (plasma frequency) and relaxation time, the conductivity is weakly dependent on Z (Fig. 3, *Bottom Left*). For $Z < 0.35$; R-square becomes negative.

In Fig. S7, we show that a dissociation fraction of 5–10% of the carrier density, inferred from shock experiments by Weir et al. (6) at similar densities and temperatures, cannot fit the energy dependency of the measured reflectance. A substantially higher dissociation fraction is required to explain the high reflectance.

Drude and Smith–Drude Conduction Model

A common assumption in optical conductivity experiments is that the optical constants determined at the measured frequencies (1.2–2.33 eV in our case) are the same as those at low or zero frequencies. In the Drude free-electron model, this assumption means that the determined relaxation time τ (1.2–2.33 eV, where the data are very well described by the Drude model) is equal to τ at $\hbar\omega = 0$ eV. However, to study possible deviation from this scenario at energies lower than 1.2 eV, we have analyzed our data using the empirical SD model for conduction in liquid, disordered, or poor metals (21). The SD model was initially proposed to account for the anomalous optical conductivity of liquid mercury in the mid-IR, and has since been applied to poor/dirty metals. It introduces a backscattering term, c, to the Drude-generalized formalism, which shifts the oscillator strength away from zero frequency to higher frequencies and depresses the dc static conductivity. The generalized SD form is, to first order,

$$\sigma(\omega) = \frac{ne^2\tau}{m(1-i\omega\tau)}\left[1+\frac{c}{1-i\omega\tau}\right].$$

The model contains three unknowns: τ, n, c. When $c = 0$, this formalism reduces to the Drude formula, $\sigma_{Drude}(\omega) = ne^2\tau/m(1-i\omega\tau)$, which in the static dc limit, gives

$$\sigma_{Drude} = \frac{ne^2\tau}{m}.$$

We would like to investigate if a fit of our data is possible that reproduces our measured wavelength dependence of the optical conduction over the range of 1.2–2.33 eV, and yet have a dc conductivity that differs from the Drude model. We found that no set of values of τ, n, c could do this. We have thus relaxed that restriction and required that the putative shifted peak due to backscattering is lower than 1.2 eV (our lowest measured energy) and it matches the measured value for optical conduction, i.e.,

$$\sigma_{Drude}(1.2\text{ eV}) = \sigma_{Smith-Drude}(1.2\text{ eV}).$$

A limited range of values for c, Z, and τ was found that could satisfy these two conditions. In Fig. S8, we plot the real part of the optical conductivity of the Smith–Drude model using this expression:

$$\sigma_{Smith-Drude}(\omega) = \frac{ne^2\tau}{m(1+\omega^2\tau^2)}\left[1+\frac{c(1-\omega^2\tau^2)}{(1+\omega^2\tau^2)}\right],$$

for $c = -0.53$, $\tau = 4.53 \times 10^{-16}$s, and $Z = 0.334$ in comparison with the Drude free-electron model. Higher values of Z, up to 0.41, could exist for slightly lower c, and τ as low as 3.8×10^{-16} s. The two most important results are, first: even within the SD model, a very high dissociation fraction is needed to account for the observed reflectance in the infrared. Second, the dc conductivity is only lower by 15–20% from our quoted values in the Drude free-electron model. As c goes to zero, the Drude free-electron behavior is recovered. We conclude that a deviation from the Drude behavior at lower frequencies is unlikely to change our main conclusions based on the Drude model.

Thermal Excitation in Semiconducting Hydrogen

Previous shock-wave experiments (4, 6) have suggested that dense fluid hydrogen at P-T conditions similar to that of our experiment is a semiconductor with a finite gap E_g of 0.3–0.4 eV. Additionally, it was argued that conduction is caused by thermal excitation of the localized carriers across that gap. We have thus calculated the reflectance signal due to free electrons for bulk hydrogen as a function of T if it were intrinsically semiconducting, to contrast it with our observed reflectance measurements (Fig. 1). In semiconductors, thermal excitation of carriers from the valence band to the bottom of the conduction band depends both on the density of available states in the conduction band and the probability of occupation as described by the Fermi–Dirac integral, given by $f_m[x] = 2/\sqrt{\pi}\int_0^\infty y^m/(1+e^{y-x})dy$. The free-carrier concentration in the conduction band is $n_i = N_S f_{1/2}[-E_g/2K_BT]$, where N_s is the number per unit volume of effectively available states, given by $2(m_{eff}K_bT/2\pi\hbar^2)^{3/2}$. Once n_i is known, the index of refraction and Fresnel reflectance as a function of T can be calculated using the same formula provided in the main text. We have assumed that the gap does not change significantly over a temperature range of 0.3 eV, as was also inferred in previous shock analysis. We used a relaxation time similar to that determined from our data to make the comparison simpler. However, the overall qualitative behavior (reflectance and dependence on T) is rather

weakly dependent on either choice. The result is shown in Fig. 1 and cannot fit our reflectance data.

Minimum Metallic Conductivity and Mean-Free Path

In the Ioffe–Regal limit (39), the mean-free path (mfp), the average distance electrons travel between collisions, cannot be smaller than the interatomic distance, a. This limit defines the MIR minimum metallic conductivity (14) and is given by $\sigma_{min} = e^2/3\hbar a$, where $\hbar$ is the reduced Planck's constant, and $a \sim (n_i)^{-1/3}$ is the interparticle spacing with n_i being the ion density.

For metallization in the molecular phase, initially suggested by Weir et al. (6), one electron per molecular ion contributes to conduction, so at the metallization pressure of 140 GPa, the density from ref. 40 is 0.385 mol/cm^3, corresponding to a molecular number density of 2.318×10^{23} molecules/cm^{3}giving $a = 1.628$ Å. In this scenario, $\sigma_{min} \sim 4{,}984$ S/cm. If metallization occurs in the atomic phase, where the molecules are fully dissociated, then the carrier density is twice as high as in the molecular phase, 4.6×10^{23} atoms/cm^3, and $\sigma_{min} = 6{,}280$ S/cm. Our conductivity results are consistent with metallization in the higher carrier density atomic phase.

The mfp is generally assumed to be $v_f \times \tau$, where v_f is the Fermi velocity and τ is the relaxation time. At the metallization density of 0.385 mol/cm^3, τ is determined from reflectance data to be $\sim 1.2 \times 10^{-16}$ s and the mfp is about 3.317 Å compared with an interatomic spacing, $a \sim 1.29$ Å.

The Free-Electron Model

The Drude free-electron model is a fundamental approach to studying equilibrium transport properties of conducting systems. Indeed it has been successfully employed to describe reflectance measurements (optical conduction) in shocked compressed water (41), helium (42), fused silica (43), diamond (44), LiF (45), Al_2O_3 (45), and hydrogen (15, 17, 18, 46) at more extreme conditions, up to 20 Mbar and 20,000 K. Unlike all of these previous cited shock-wave experiments, which relied on a single-wavelength reflectance measurement and simply assumed the applicability of the Drude model, we have measured reflectance at multiple wavelengths over a region of 1–2.33 eV and conclusively established a distinct free-electron behavior. That is, the LMH reflectance increases as a function of increasing wavelength. The wavelength dependence observed is well described by the Drude model (see fit in Fig. 2 and Fig. S6).

Theoretically, the free-electron model is applicable when the electron subsystem is both degenerate, that is $T << T_f$ and the ratio of a dimensionless $\hbar/\varepsilon_f\tau$ is less than unity, where $\varepsilon_f = 16.4$ eV is the Fermi energy at 140 GPa (2,500 K). The second criterion is related to the Boltzmann conduction transport theory, where the scattering of electrons off ions is assumed to be a weak quantum perturbation to the system. In our experimental conditions, both of the above criteria are very well satisfied.

An interesting result from our current data is that close to the metallization boundary, where reflectance is steeply rising, the energy dependence of this measured reflectance cannot be described by the Drude model in its simplest terms. Additional terms that accounts for partial ionization (low density of carriers accounting for the lower reflectance) or the effects of core electrons might be needed to provide a more accurate description of the reflectance in that region.

Uncertainties in the Dynamic Shock-Wave Conductivity Experiments

In the four-probe arrangement used in the 1996 shock-wave conductivity experiments, a calibration calculation is used to determine the cryogenic sample cell dimension at different compressions (4, 6). This calibration calculation is used to relate the measured resistance value to the reported resistivity at these compressions. These calculations assume an equilibrium current density over the cross-sectional area of the two current measuring electrodes, i.e., that the electrodes are flush at the sapphire anvil/hydrogen interface. However, as noted in Nellis et al. (4), the electrodes intrude into the hydrogen samples "a few 10 μm" because of different shock impedances of steel and sapphire. This is comparable to the sample thickness of 50 μm, and can perturb the current density leading to additional uncertainty in the conductivity. This could possibly explain the difference between our determined conductivities and those earlier reported by Weir et al. (6).

Calculations of the microtransport properties of LMH relevant to planetary conditions are provided below.

Conductivity of Hydrogen–Helium Mixture

The addition of helium to the metallic fluid could decrease the conductivity by adding more scattering centers. However, Lorenzen et al. extensively studied transport properties of hydrogen–helium mixtures as a function of helium fraction for similar conditions to those experimentally reported here (47). They showed that the addition of 8.57% helium to a conducting hydrogen fluid, the mean protosolar value, only decreases the mixture conductivity by 20–25%. This should be compared with our quote uncertainty of 15%. As the helium fraction increases, the drop in the conductivity is more pronounced. However, at much higher P-T conditions, helium is expected to contribute to conduction of the mixture.

Magnetic Reynolds Number and Magnetic Diffusivity

In magnetohydrodynamics, the electrical conductivity σ is usually expressed in terms of the magnetic diffusivity β with $\beta = 1/\mu_0\sigma$, where μ_0 is the magnetic vacuum permeability.

The important quantity in dynamo action theory is the magnetic Reynolds number R_m, which assesses whether the dynamo action at a certain depth is possible. R_m measures the ratio of magnetic field production to Ohmic dissipation and is equal to $R_m = v_{conv}L/\beta$. Here, v_{conv} is the convective flow velocity, β is the magnetic diffusivity, and L is the characteristic length scale for the conducting core. Dynamo numerical simulations suggest that R_m must typically exceed 50 to guarantee dynamo action (48). In the regime where the magnetic field is generated, v_{conv} is predicted to be in the range of ~0.1–1 cm/s (9). Since L is of the order of a few 10^9 cm, the largest acceptable value for β is $\sim 10^7$ cm^2/s for the outermost dynamo generating region. For the conductivities observed in our experiments, $\beta \sim 0.56 \times 10^4$ cm^2/s at pressures corresponding to 0.84 of Jupiter's radius and 0.64 of Saturn's radius (25). The addition of 10% helium is unimportant for these conductivity estimations, since at these P-T conditions helium still has a rather high ionization potential (26). We note that these values are now very similar to recent estimates for the Earth iron core mantle boundary, yielding $\beta \sim 0.59 \times 10^4$ cm^2/s (49).

If metallization and dissociation occur continuously through the Jovian isentrope, then the depth, corresponding to $\beta = 10^7$ cm^2/s, is more likely shallower than previous estimates and may well extend to more than ~0.91 R_J. This region is at roughly 7,000 km depth and corresponds to where the Jovian isentrope intersects the 50% dissociation line of hydrogen predicted by the DFT calculations (26). We note that these values are larger than most previous estimates that place the source region of the Jovian dynamo at depths of 0.85–0.8 R_J (28–30) and much larger than the usual definition of the Jovian metallic core (9).

Thermal Conductivity

For degenerate simple metals at high temperatures, thermal conductivity λ is dominated by electronic transport. The relation between electrical and thermal conductivity in metals should be well described by the Wiedemann-Franz law. Using the Lorentz number L_0 as a proportionality constant, $\lambda = \sigma L_0 T$, where T is the

temperature in kelvin. At conditions of the Jovian interior (4,000 K and 140–170 GPa), $\lambda \sim 100$–140 W/mK. We note that there could be some systematic uncertainty due to the unknown dependence of σ of LMH on temperature, although most theoretical treatments either assume or have shown some weak dependence. The ionic contribution to the thermal conductivity is known to be rather small and can be ignored. Our value is in very good agreement with recent theoretical calculations of λ for LMH (3) but higher than those calculated along Jovian adiabat (26).

Thermal Diffusivity

The important quantity that characterizes heat transport is thermal diffusivity, which is given by $\kappa = \lambda/\rho C_p$, where C_p is the specific heat capacity at constant pressure and ρ is the density in gm/cm^3. In the high-temperature limit for liquid metals, C_p can be assumed to be $3NK_B$ where N is the ion density at the conditions of our experiment and K_B is the Boltzmann constant. Like the conductivity, thermal diffusivity is dominated by electronic transport in a degenerate system, $\kappa \sim 1.3 \times 10^{-5}$ m^2/s.

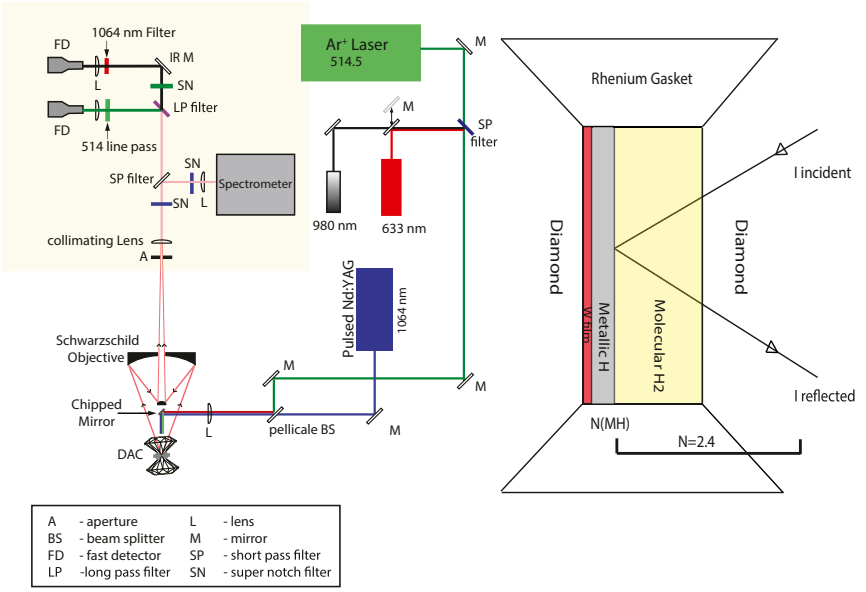

Fig. S1. (*Left*) Experimental layout used in the current experiments to simultaneously measure optical reflectance at two different laser frequencies as a function of *T*. In our previous experiments (16), only one laser-light measurement was possible at a time, rendering accurate large uncertainties in determination of the optical constants. (*Right*) A schematic of the DAC interior showing the arrangement of reflectance measurements. The interfaces between the layers are to a very good extent specularly smooth. At the experimental conditions, the diamond and the molecular hydrogen layer have approximately the same index of refraction. Estimation of the thickness of each layer is provided in the text.

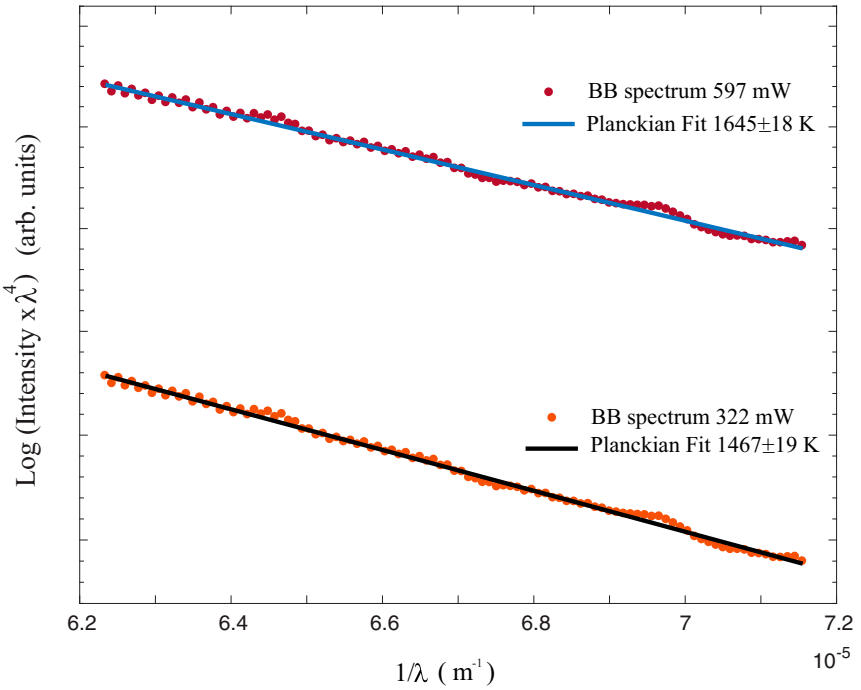

Fig. S2. Thermal radiation spectra for two different laser powers below and above the metallization transition at 140 GPa. Spectra were normalized by the transfer function and then fitted to the Planckian function in the range of 1.3–1.7 μm. The resultant fits and the uncertainties are shown.

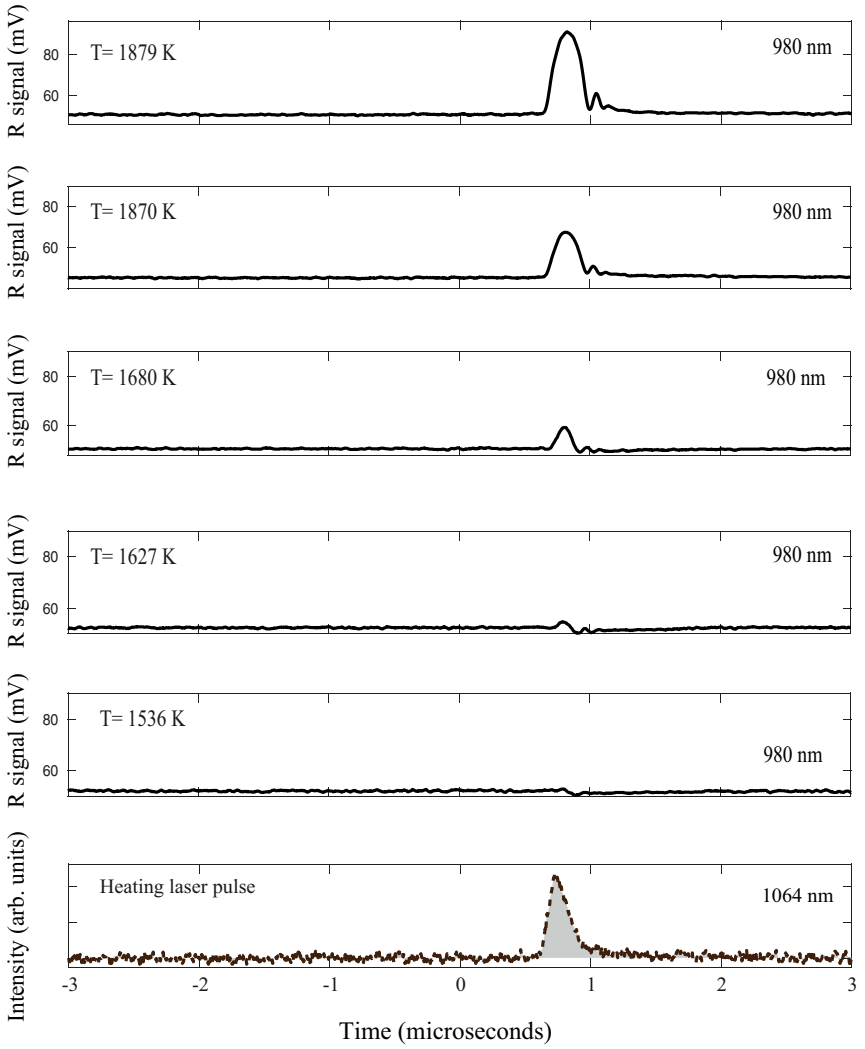

Fig. S3. Example of the raw time-resolved reflectance traces recorded as a function of temperatures and time for 980-nm light and $P = 140$ GPa. (*Bottom*) Timing of the heating laser pulse, 1,064 nm. Above a certain temperature, fluid hydrogen abruptly metallizes and reflects the incident probe light. The secondary peaks are due to interference in the metallic deuterium/diamond interfaces.

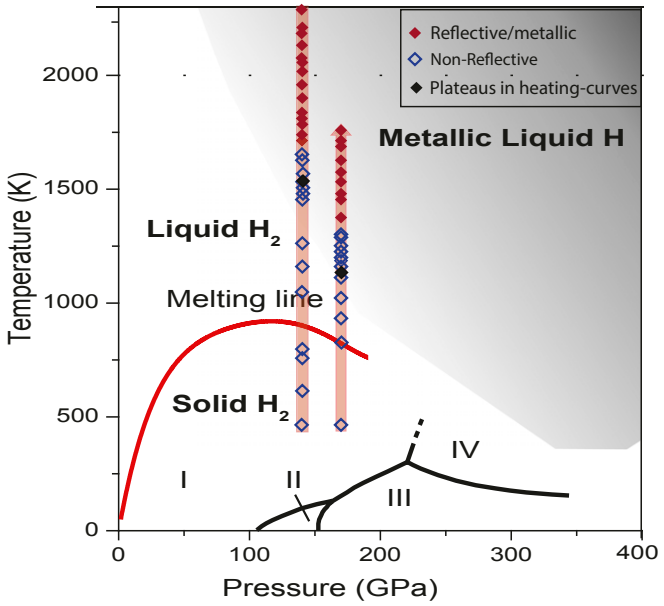

Fig. S4. Phase diagram of hydrogen showing the thermodynamic pathway (thick arrows) used for the current measurements. The blue data points correspond to zero reflectance reported from this work and earlier (16), while red points denote the reflective state. The black data points from ref. 16 correspond to the observation of the plateaus in heating curves.

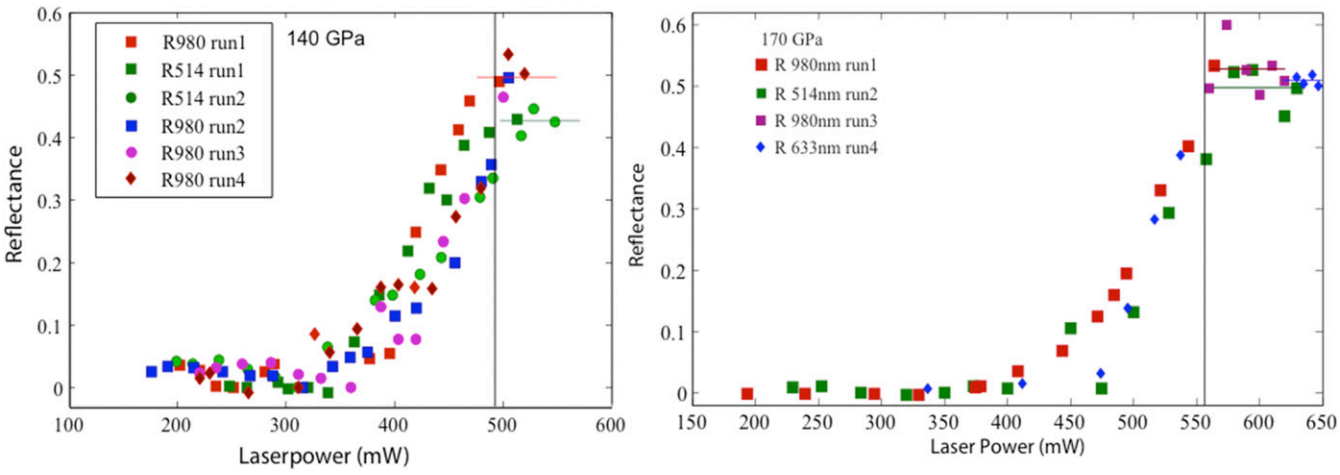

Fig. S5. Raw reflectance data as a function of laser power collected at eight runs for different wavelengths. The vertical black solid line denotes the region where the metallic hydrogen layer reaches the bulk limit at which reflectances saturate. The horizontal lines are guides to the eye for the average value of this reflectance saturation for respective wavelengths.

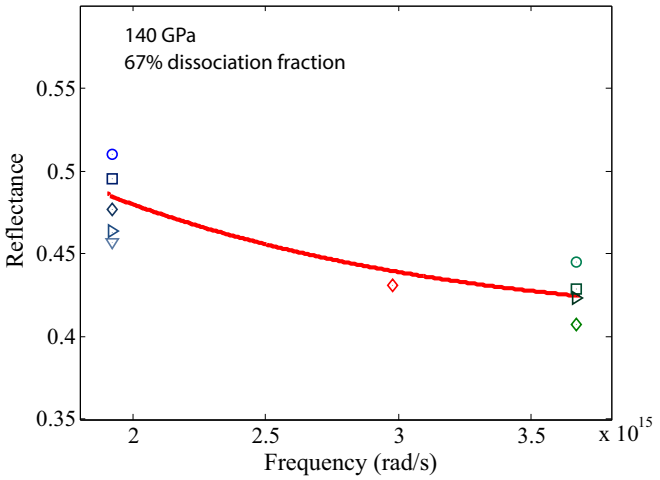

Fig. S6. LMH reflectance data at 140 GPa as a function of angular frequency fitted to the Drude reflectance formula to extract the Drude parameters: plasma frequency and relaxation time. The data used for the fit are the reflectance points shown in Fig. S3 to the right of the vertical line, corresponding to reflectance saturation.

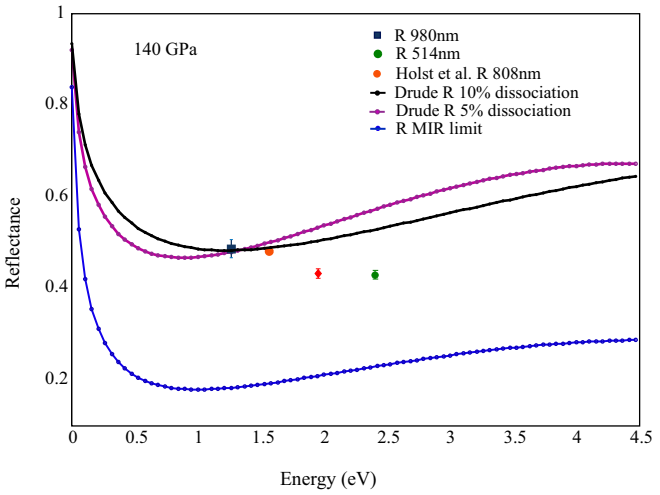

Fig. S7. LMH reflectance data as a function of energy at 140 GPa. Two different Drude reflectances are calculated for 5% and 10% dissociation fraction reported at ref. 6. We show that irrespective of our choice of τ, a small dissociation fraction cannot fit the energy dependency of our reflectance data. The calculated reflectance using the MIR limit is plotted for comparison.

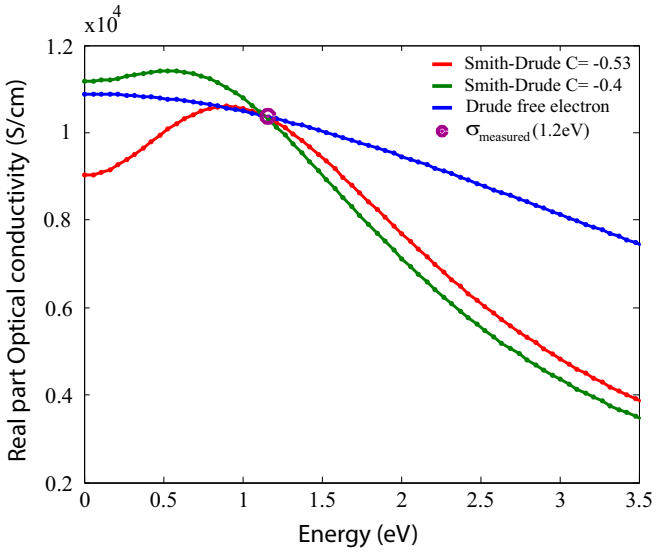

Fig. S8. Real part of the dynamic conductivity plotted as a function of energy using the SD model for different *c* values compared with the Drude free-electron model. Notice that as *c* increases, the infrared peak shifts to lower frequencies and the optical conduction becomes more Drude-like. The purple point is the optical conductivity datum from the reflectance measurement at 1.2 eV.